Fuel 302 (2021) 121178

Contents lists available at ScienceDirect

Fuel

journal homepage: www.elsevier.com/locate/fuel

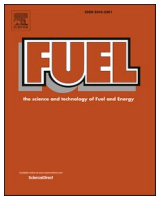

Full Length Article

Inverted U-shaped permeability enhancement due to thermally induced desorption determined from strain-based analysis of experiments on shale at constant pore pressure

Brandon Schwartz *, Derek Elsworth

Department of Energy and Mineral Engineering, EMS Energy Institute and G3 Center, Penn State University, University Park, PA, USA

ARTICLE INFO

Keywords:
Shale permeability
Thermally induced desorption
Sorptive strain in shales
Shale mineralogy
Shale rheology
Adsorption in shale

ABSTRACT

We explore the impact of thermally induced desorption on permeability evolution in shale at constant pore pressure. Permeability loss due to thermal expansion of mineral aggregates competes with permeability enhancement due to thermal desorption and shrinkage with increasing temperature. In experiments using core plugs of Marcellus shale, permeability increases 20% from 296 to 322 K for a pre-fractured sample and 11% from 304 to 334 K for an intact sample. Dynamic bulk modulus decreases from 14.6 to 11.8 GPa when permeability increases from 2.8 to $3.1{\cdot}10^{-21}$ m^2, suggesting that pore volume is expanding due to desorption. We develop a model for thermal-sorptive permeability enhancement that accounts for pore evolution due to overprinted but competitive thermal and sorptive strains. A scaling factor between 0 and 1 is included to account for the volumetric boundary condition ranging from free boundary expansion to fixed bulk volume. The change in fracture aperture is directly impacted by fracture density. While permeability evolution in shales is generally characterized by a "U" shaped behavior with increasing pore pressure, our model shows that thermally induced permeability evolution at constant pore pressure is characterized as an inverted "U". This is due to permeability enhancement at temperatures close to the reference temperature and permeability loss at higher temperatures. We attribute this to larger changes in adsorbed volume at lower temperatures competing with linear thermal strain that then outpaces desorption at higher temperatures. Both thermal and sorptive strains are modulated by the mineral distribution within the shale. Discretized images of mineral distribution suggest that there may be a larger local permeability enhancement than predicted by bulk strain measurements alone, due to the concentration of porosity near sorptive components. Our results include a novel analysis of permeability evolution due to desorption at constant pore pressure.

1. Introduction

Shale is a sedimentary rock composed primarily of clays, silicates, carbonates, and organic matter [54]. Shale is typified by low permeability which can be 10–100 times lower in the bedding-perpendicular direction than in the bedding-parallel direction [4,27,39]. This permeability anisotropy is due to the concentration of porosity between clay-mineral laminae parallel to bedding [55,19]. Flow paths parallel to bedding are characterized as macropores and long microfractures that create a preferential flow network through the shale [38,24]; Yan et al., 2015; [13]. In between laminae, fluid transport originates in nanopores and is driven by diffusion [21,22,8]. Both parallel- and perpendicular-to-bedding, storage and flow occur predominantly in the kerogen and clay components [53,12]. Imaging of kerogen in shales shows a spongelike network of nanopores that create high surface area for sorptive storage [23]. This arrangement leads to nanoscale diffusion out of the kerogen into micro-fissures and bedding-parallel fractures during fluid flow [59,15,35].

While it remains challenging to image nanopores, the pore volume of the preferential flow network is sufficiently large that it is readily imaged using numerous techniques [18,11,17]. In all cases, imaging techniques reveal planar microfractures and macropores separating laminae. Because gas flow in shale originates in nanopores and within laminae along clay platelet boundaries, permeability models must account for the diffusion-driven flow that occurs in these spaces [6,5]. As the gas approaches the bedding-parallel flow paths, fluid transport

* Corresponding author.
E-mail address: bos5313@psu.edu (B. Schwartz).

https://doi.org/10.1016/j.fuel.2021.121178
Received 3 February 2021; Received in revised form 17 May 2021; Accepted 30 May 2021

begins to transition to the Darcian flow regime. This necessitates dual permeability models that can couple Fickian and Darcian flow when considering field-scale response [30]. In the laboratory, however, shale permeability is generally measured individually in either bedding-parallel or -perpendicular directions using pressure pulse tests (Brace, 1968). As a result, measurements taken in the bedding-parallel direction are measuring the permeability of the system of planar microfractures and macropores that make up the preferential flow network.

The large aperture of flow paths in the preferential flow network allows for use of the cubic law to model permeability [58,1,20]. Permeability evolution in fractured, sorptive media is typically cast as an ensemble response to evolving strains [34,57,47], and these strains are often competitive with each other [36,50]. For example, thermally induced permeability evolution in coals is modeled as an ensemble response to thermal and sorptive strains and dependent on applied boundary conditions [42]. While there are several differences between shale and coal—namely the %TOC, the nature of the flow paths, and the distribution of minerals—shale should have a similar response.

Thermal strain causes minerals to expand with increasing temperature with expansion coefficients of the composite mineral aggregates of the order of $\sim 10^{-5}$/K [43]. Shales experience traditional thermal expansion in the range 300–400 K typical of reservoirs [16] but at ~ 470 K they begin to collapse as kerogen undergoes pyrolysis and illitic clays experience a reduction in spacing between platelets (Weaver and Pollard, 1973). Thermal expansion of shales comprising multi-mineralic aggregates is lower than that of its individual mineral components [43] as pores and cracks reduce skeletal stiffness and reduce aggregate thermal expansion coefficient to be less than that of the weighted average of its mineral composition [10]. The difference is due to mineral expansion being distributed partly to bulk volume expansion and partly to pore closure, indicating that thermal strain reduces permeability. The magnitude of permeability loss depends on the percentage of mineral expansion that contributes to pore volume reduction. Thermal strain significantly reduces permeability for constant volume reservoirs [41] – one end member behavior for the spectrum of boundary conditions. However, increasing temperature also causes desorption in sorptive rocks that can both lead to permeability enhancement [46,31] or permeability loss [51] depending on the comparative influence of the competitive thermal and sorptive strains.

Adsorption in clays and organic matter causes sorptive swelling, leading to volume expansion measured as sorptive strain [28]. Sorptive storage accounts for most of the gas in place in organic-rich shales [37]. Sorptive swelling also constricts flow paths internally, which causes permeability loss with increasing adsorption [33]. In this regard, sorptive swelling is similar to thermal expansion. The most common way to increase the amount of adsorbed gas is to increase the pore pressure. Adsorption in shales typically follows a Langmuir adsorption model which is typified by large incremental increases in fractional coverage of adsorption sites at low pressures progressing to smaller incremental increases in fractional coverage of adsorption sites at high pressures. The adsorbed volume at 100% monolayer coverage is known as the Langmuir volume. The sorptive strain increases linearly with fractional coverage [44], with the maximum strain called the Langmuir strain.

The large increase in sorptive strain at low pore pressures causes permeability loss [26]. As increasing pore pressure begins to cause less additional fractional coverage, poromechanical expansion begins to outpace sorptive permeability loss. This permeability loss, followed by permeability recovery and enhancement in shales and coals, is typified by a "U" shaped change in permeability with increasing pore pressure [57]. When the sorptive permeability loss is isolated from poromechanical expansion, it is shown to have a Langmuir signature [50]. Desorption of methane typically increases permeability in shales as sorptive swelling is reduced [32]. Desorption induced permeability enhancement occurs during nonsorptive gas flooding in shales as the partial pressure of the methane is reduced at constant temperature [50]. However, the Langmuir isotherm model predicts that desorption also occurs with increasing temperature at constant pore pressure. This leads to counterintuitive mechanical behavior in sorptive rocks with increasing temperature. Rock stiffness in shales tends to decrease upon heating and increase upon cooling [9,64]. Laboratory tests on European black shales show that rock stiffness decreases with increasing temperature in single stage uniaxial compression tests [45]. Increasing temperature leads to a softening of coals, indicated by a decrease in bulk modulus [25]. Pore closure causes the dynamic bulk modulus to increase as the shale becomes stiffer due to decreased porosity [48]. The effects of temperature on mechanical property evolution and permeability evolution of shales are areas of continuing research.

To address these unknowns, we explore the relationship between sorptive strain and thermal strain in shale at constant pore pressure. Both strains are dependent on mineral distribution, which we characterize through imaging techniques. We measure permeability evolution with changing temperature for samples of Marcellus shale while recording changes in dynamic bulk modulus. We build a model for permeability evolution as a function of evolving thermal and sorptive strains. The impact of fracture density, boundary constraint and competitive swelling are explored.

2. Characterization techniques

To inform model development we first characterize a sample of Marcellus shale using scanning electron microscopy (SEM) with light elemental analysis to understand mineral property distribution. Then we perform experiments with varying pore pressure and temperature to observe changing internal pore structure *via* gas permeability measurements. We perform experiments on both a pre-fractured core plug and an intact sample containing no large fractures. Fig. 1 shows the characterization workflow, with anticipated results including permeability enhancement due to gas desorption in competition with permeability reduction due to mineral expansion with increasing temperature.

2.1. Imaging techniques

We prepare samples of Marcellus shale cored perpendicular to (across) bedding using ion milling parallel to bedding. We load the core into a scanning electron microscope (SEM) with light elemental analysis capabilities. Fig. 2a shows a backscatter image approximately 0.2x0.2 mm with dark areas of organic matter visible in the center. Framboidal pyrite is visible as small, bright dots throughout the image. Other minerals typically found in the Marcellus shale include illite, smectite, silicates and calcite. We use light elemental analysis to identify pixels containing predominantly carbon, oxygen, silicon, calcium, aluminum, and other elements found in minerals common to shales. The elemental maps are imported as 800x1040 arrays of pixels into MATLAB to identify grain boundaries. While grain interiors are straightforward to identify, digitizing the edges is more challenging. After delineating appropriate boundaries using changing mineralogy, we refine the edge identification manually. Future work to fully automate image discretization is planned. Once grains are identified, mineralogy is assigned based on the elemental maps. Fig. 2b shows calcite, quartz, and organic matter in a clay matrix. We ignore pyrite. By area, the image is 47.7% clays, 5.63% organic matter, 35.08% carbonates, and 11.58% silicates. XRD analysis shows the broader interval is 38.2% clays, 1.0% organic matter, 34% carbonates, and 19.9% silicates, suggesting good agreement between these methods.

We further enhance the digital image by assigning coefficients of thermal expansion. We use generally accepted coefficients of thermal expansion for illite, quartz, calcite, and kerogen, which range from 2 to $10{\cdot}10^{-5}$/K [43]. Fig. 2c shows the distribution of thermal expansion coefficients. Additionally, we assign sorptive affinity to each mineral in Fig. 2d. We note that the organic matter has the highest affinity to adsorption. Clays are weakly sorptive, but also make up a larger percent of the area of the image. Silicates and carbonates are non-sorptive.

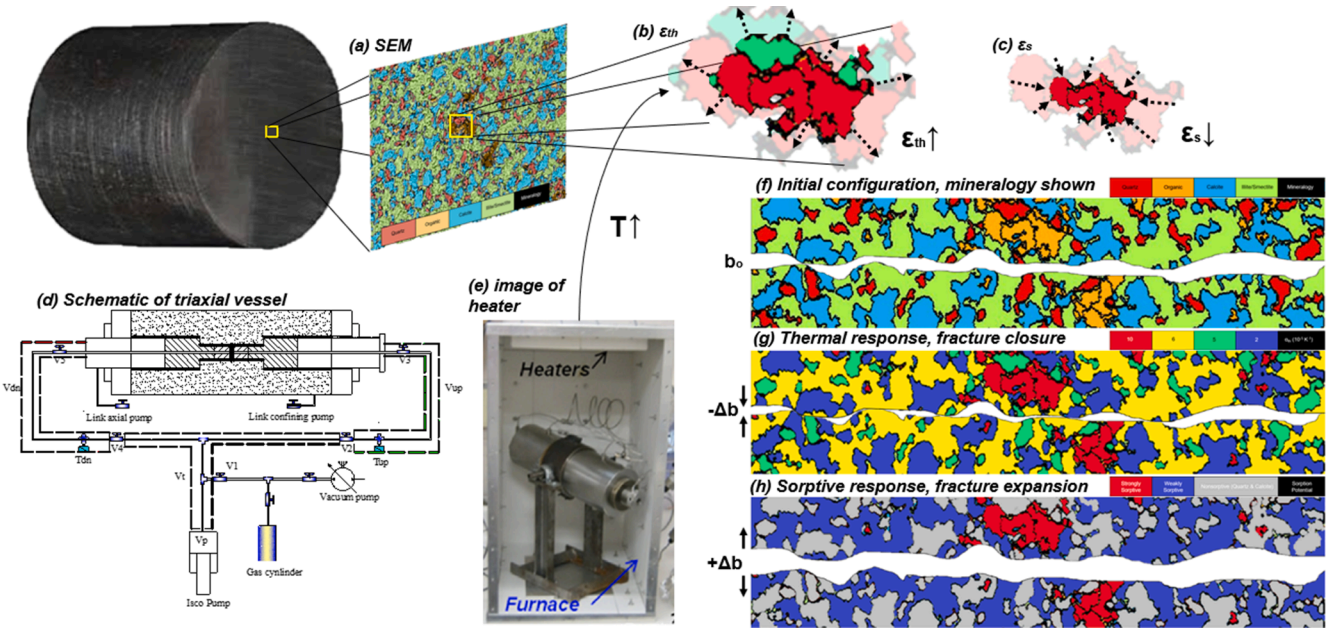

Fig. 1. Model Illustration. Samples are characterized using imaging techniques (a). The impact of evolving thermal and sorptive strains (b-c) are measured with experimental techniques (d-e) to inform thermal-sorptive model development. Changes in permeability are due to microfracture closure/expansion (f-h). Colors in (f-h) correspond to Fig. 2.

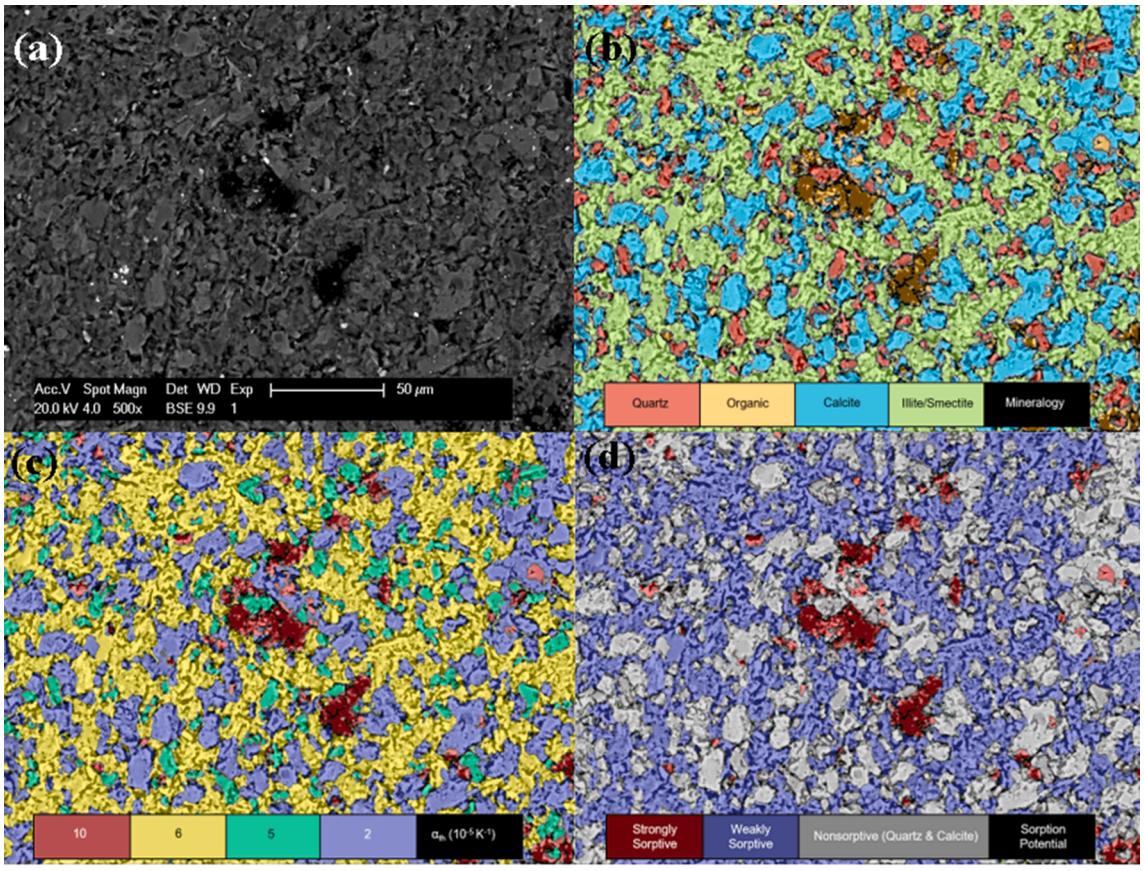

Fig. 2. SEM image showing rock fabric *via* backscattered electrons (a), digitized grain boundaries and mineral distribution (b) and thermal expansion (c) and sorptive affinity (d) maps.

2.2. Experimental techniques

Using the same interval of the Marcellus shale, we separately load contrasting fractured and un-fractured core plugs into a triaxial vessel which is placed within a furnace (Fig. 1). After applying a hydrostatic external stress of 24 MPa, we allow each core plug to compact over

several days. Once the core plug stops deforming, as measured within +/- 0.1 μm by a linear variable displacement transducer (LVDT), we serially inject sorptive then nonsorptive gas species while measuring permeability evolution with changing pore pressure. After a set of permeability measurements is taken for methane and helium over a range of pore pressures, we increase the furnace temperature and repeat the permeability measurements. Overall, pore pressures are varied from 1 to 8 MPa and temperature is varied from 296 to 335 K. To minimize the effects of free gas expansion, we plot each set of measurements at constant pore pressure. This isolates the sorptive strain by minimizing the strain caused by the free gas. As the experiments are held at constant stress, the slight expansion of gas due to the ~ 10 K increase in temperature is allowed to dissipate and should also have minimal contribution to strain measurements. Temperature is allowed to equilibrate to the next set point overnight and held constant during measurements, reducing measurement uncertainty due to ambient fluctuations. Pressure pulse tests calculate permeability by measuring the slope of the pressure decay as described in Brace (1968), but the R^2 value of the slope can be low in permeability measurements with shale. All pressure decay measurements in our experiments have R^2 values greater than 0.95, indicated a goodness of fit that minimizes permeability measurement uncertainty.

2.2.1. Permeability through a fracture of known dimensions

To establish permeability evolution in shale fractures with a known initial aperture and fracture spacing, we fracture a core plug 19 mm in diameter. Fig. 3 shows an image of the core plug face overexposed to emphasize the fracture. The fracture geometry is not planar. We measure permeability enhancement with increasing temperature using both methane and helium. The initial permeability is $6.7{\cdot}10^{-18}$ m^2. The diameter of the core plug and the initial permeability can be used to solve for initial fracture aperture:

$$b_o = \sqrt[3]{12ks} \tag{1}$$

where k is the initial permeability and s is the diameter of the core plug. Since the diameter of the core plug is 0.019 m, the initial aperture is 1.15 μm and the ratio of fracture spacing to fracture aperture s/b is ~16,500.

After measuring initial permeability, we vary temperature and pore pressure to create isobars of permeability evolution with changing temperature. We normalize permeability as k/k_0 where k_0 is the first permeability measurement and plot results in Fig. 4. For methane, Fig. 4a shows permeability enhancement with increasing temperature for all isobars due to desorption within clays and organic matter and thermal expansion of the bridging asperities. Fig. 4b shows helium permeability enhancement due to thermal expansion along the nonplanar fracture geometry. Permeability evolution is shown for three different isobars at 1 MPa, 2 MPa, and 3 MPa. The permeability enhancement for methane is larger than the permeability enhancement for helium, suggesting desorption along clays and organic matter.

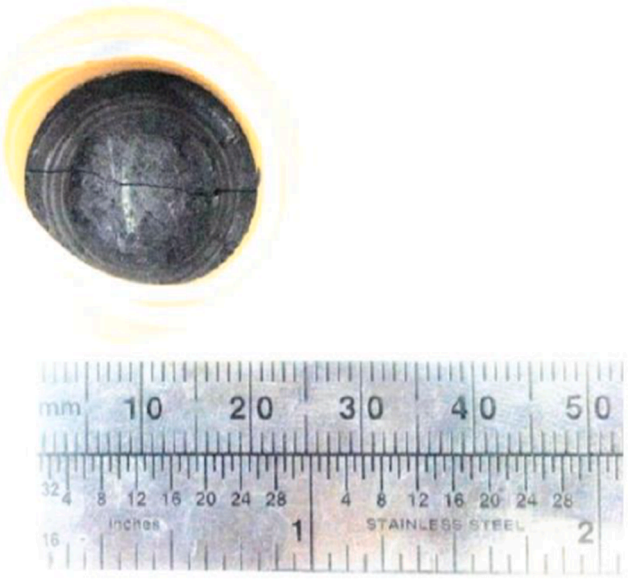

Fig. 3. An overexposed image of fractured core plug. The plug is 19 mm in diameter.

2.2.2. Permeability through an intact sample

After measuring methane permeability of a pre-fractured sample, we repeat the experiment with an intact sample. We concurrently measure dynamic bulk modulus during permeability measurements using piezoelectric transducers (PZTs). Initial permeability of the intact sample is 2.8 nanodarcies, or $2.8{\cdot}10^{-21}$ m^2. From 305 to 335 K, permeability increases approximately 11%. Fig. 5a shows permeability enhancement with increasing temperature, suggesting that pore dilation from thermally induced desorption has a larger local effect than pore closure from mineral expansion. Fig. 5b shows that as permeability decreases, measurements of dynamic bulk modulus increase. Dynamic bulk modulus decreases from approximately 14.6–11.8 GPa while permeability increases from approximately $2.8–3.1{\cdot}10^{-21}$ m^2. This is consistent with the rock becoming softer as pores dilate. Dynamic bulk modulus decreases with increasing temperature as pores dilate from additional desorption.

3. Theory

Next, we present a novel analysis of isobaric sorptive behavior by extracting the change in fractional coverage of sorption sites with changing temperature for various Langmuir isobars. Then, we develop a model to predict permeability evolution with increasing temperature that accounts for thermal expansion and sorptive shrinkage. Lastly, we apply the model to permeability enhancement observed in shale due to thermally induced desorption in laboratory experiments. Table 1 summarizes the nomenclature used for model development.

3.1. Isobaric desorption

In the Langmuir adsorption model, adsorption is cast as a function of increasing pore pressure at constant temperature. These Langmuir isotherms are illustrated in Fig. 6a as increasing fractional coverage of available adsorption sites. When derived from a kinetic framework, the Langmuir equation for fractional coverage may be defined as [14]:

$$\theta = \frac{bP}{1 + bP} \tag{2}$$

where θ is the fractional coverage and P is pressure. The affinity constant b is in units of Pa^{-1} and is

$$b = b_\infty e^{Q/RT} \tag{3}$$

where b_∞ is the affinity constant at infinite temperature, Q is the heat of adsorption, R is the universal gas constant, and T is temperature. The value of b_∞ can be extrapolated from laboratory data, and is equal to

$$b_\infty = \frac{\alpha}{k_{d_\infty}\sqrt{2\pi MRT}} \tag{4}$$

where α is a sticking (attachment) coefficient, $k_{d\infty}$ is the rate constant for desorption at infinite temperature, and M is the molecular weight of the gas. For a given gas and solid, the only variable in Eq. (4) is T, such that b_∞ varies with $T^{-1/2}$ as:

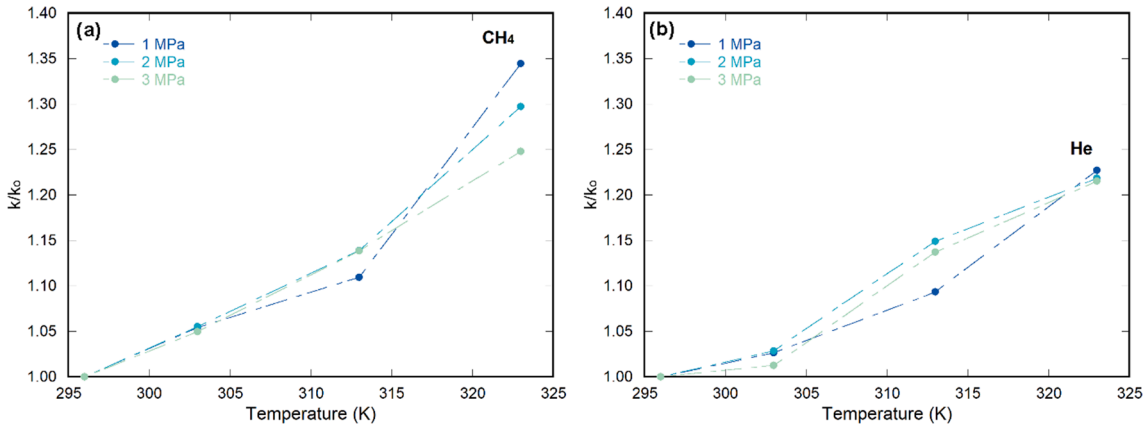

Fig. 4. Isobaric permeability evolution for methane (a) and helium (b). Methane experiences a larger permeability enhancement due to the additive impact of desorption.

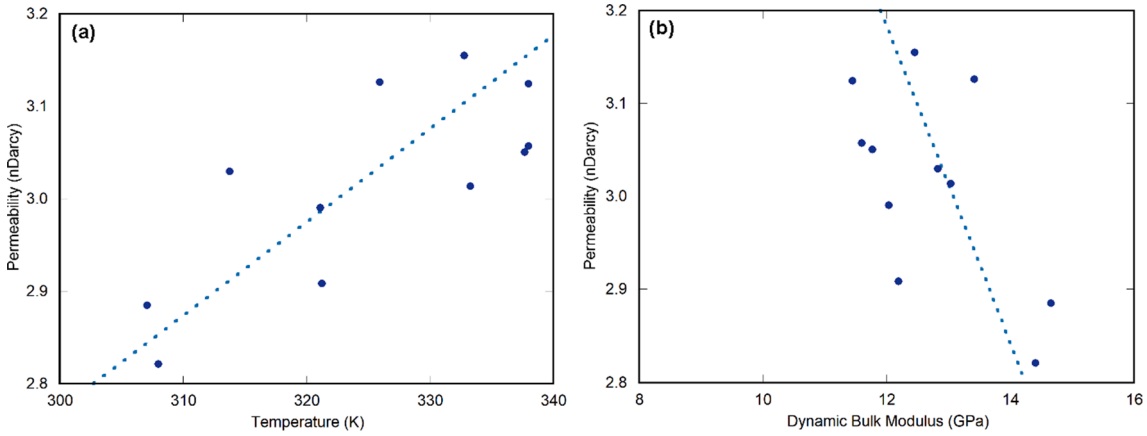

Fig. 5. Permeability enhancement with increasing temperature (a). Permeability decreasing with increasing dynamic bulk modulus (b), consistent with increasing rock stiffness due to pore closure.

Table 1
Nomenclature.

Symbol	Description	Units
b	Langmuir affinity constant	MPa^{-1}
b_0	Initial fracture aperture	m
k	Permeability	m^2
s	Pore spacing	m
$k_{d\infty}$	Rate constant for desorption	–
A	Boundary expansion factor	–
R	Universal gas constant	$J{\cdot}K^{-1}{\cdot}mol^{-1}$
P	Pore pressure	MPa
P_L	Langmuir pressure	MPa
Q	Heat of adsorption	$J{\cdot}mol^{-1}$
T	Temperature	K
M	Molecular weight	g/mol
α	Sticking coefficient	–
α_{th}	Coefficient of thermal expansion	K^{-1}
θ	Fractional coverage	-/-
ε	Strain	–
φ	Porosity	%

$$b_\infty = b_{\infty 0}\left(\frac{T}{T_0}\right)^{-\frac{1}{2}} \tag{5}$$

Sorptive strain is linear with fractional coverage [44]. With the maximum strain occurring at 100% coverage, sorptive strain is defined as

$$\varepsilon_s = \varepsilon_L \frac{P}{P_L + P} \tag{6}$$

where ε_L is the Langmuir strain at 100% coverage of sorption sites and P_L is the Langmuir pressure. P_L corresponds to 50% fractional coverage and is readily estimated from laboratory data. The Langmuir strain ε_L is typically estimated by curve fitting. Fig. 6b shows standard isotherms for sorptive strain. A comparison of Eqs. (2) and (6) shows that P_L equals $1/b$. For a given ε_L the sorptive strain can be cast as a function of varying pressure and temperature:

$$\varepsilon_s = \varepsilon_L \frac{b_\infty e^{Q/RT} P}{1 + b_\infty e^{Q/RT} P} \tag{7}$$

While Fig. 6a shows fractional coverage isotherms with varying pressure, Fig. 6c shows fractional coverage isobars with varying temperature. The region from 290 to 400 K is highlighted to show how fractional coverage changes with varying temperature at typical reservoir conditions. Q is a constant that can be measured in the laboratory. A typical value of Q for shale is 17 kJ/mol [29,7,62], which we use here. Fig. 6d shows sorptive strain isobars as a function of changing temperature when ε_L is $5{\cdot}10^{-4}$.

3.2. Thermal-sorptive permeability evolution

Permeability evolution is the result of evolving strains that impact the pore space. As a function of changing fracture aperture, permeability

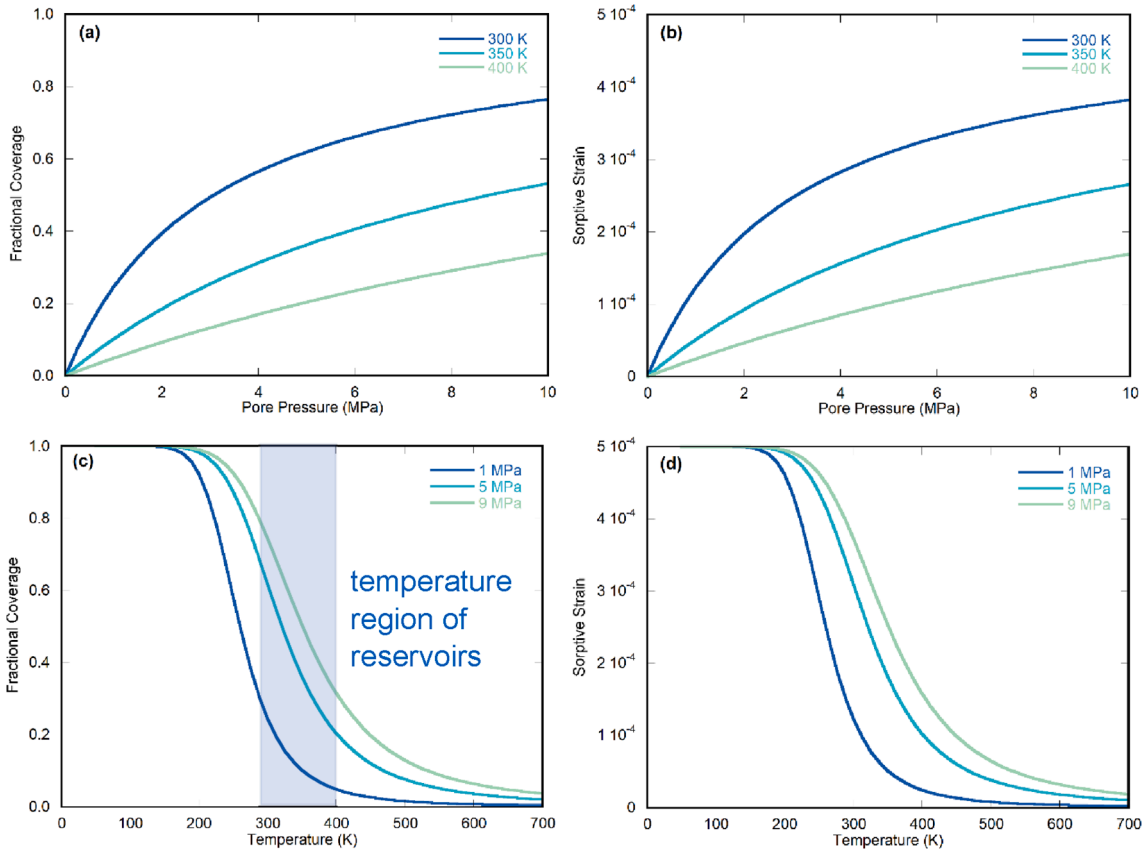

Fig. 6. Behavior of sorptive gases at constant temperature or pressure. Langmuir isotherms for fractional coverage of available sorption sites (a). Langmuir isotherms for sorptive strain (b). Isobars for changing fractional coverage, with behavior in the temperature region typical of reservoirs highlighted (c). Isobars for sorptive strain with varying temperature (d).

evolution can be normalized as

$$\frac{k}{k_0} = \left(1 + \frac{\Delta b}{b_0}\right)^3 \tag{8}$$

where k_0 is the initial permeability, b_0 is the initial fracture aperture, and Δb is the change in fracture aperture. Eq. (8) can be applied to represent multiple fracture sets where Darcy's law applies, and we use it here to model permeability evolution of the microfractures and macropores that make up the preferential flow network through the shale.

Fig. 6d shows that increasing temperature causes desorption that relaxes the sorptive strain. Desorption opens pore space as sorptive swelling is reduced [28]. Therefore, the change in fracture aperture due to desorption is

$$\Delta b_s = As\Delta\varepsilon_s, 0 \le A \le 1 \tag{9}$$

where s is the spacing between fractures while A represents the boundary condition and ranges from 0 for free expansion to 1 for fixed bulk volume. The temperature at the beginning of desorption determines $\Delta\varepsilon_s$. Fig. 7a shows desorption-driven strain for three pore pressures from a starting temperature of 300 K. The impact of thermal expansion on fracture aperture will depend on whether the boundary condition allows the shale to undergo free expansion, partial expansion, or is fully constrained and with no expansion:

$$\Delta b_{th} = -A(s\Delta\varepsilon_{th}) \tag{10}$$

where ε_{th} is the thermal strain. The negative sign indicates that mineral expansion should reduce pore volume. The thermal strain is

$$\Delta\varepsilon_{th} = \alpha_{th}\Delta T \tag{11}$$

where α_{th} is the coefficient of thermal expansion. Thermal expansion can be approximated as linear for shales in the 300–400 K range. For shale, a typical value for α_{th} is $2{\cdot}10^{-5}$ K^{-1} [43], and we use this value in our study. We note that an arithmetic average of the mineral distribution by area %, as shown in in Fig. 2c, gives a coefficient of thermal expansion of $4.5{\cdot}10^{-5}$ K^{-1}.

Eqs. (9–10) show that the sorptive strain and thermal strain are mutually competitive and thus the net response of the shale volume will depend on the sum of these two strains. Fig. 7b shows sorptive, thermal, and net strain from 300 to 340 K for three pore pressures. The thermal strain at constant temperature is identical for all three isobars, as the coefficient of thermal expansion is independent of pore pressure. Combining Eqs. (9–11), the net change in aperture is

$$\Delta b = As(\Delta\varepsilon_s - \Delta\varepsilon_{th}) \tag{12}$$

Fig. 7c shows the net change in aperture from 300 to 340 K for three pore pressures. For the 1 MPa isobar, the net aperture change is negative. For the 5 MPa isobar, the net aperture change is positive and has an inverted "U" shape as thermal strain overtakes sorptive strain. The 9 MPa isobar reflects a neutral response, where the sorptive strain and thermal strain essentially cancel each other out. Incorporating net aperture change in Eq. (8) with permeability evolution gives

$$\frac{k}{k_0} = \left(1 + A\frac{s}{b_0}(\Delta\varepsilon_s - \Delta\varepsilon_{th})\right)^3 \tag{13}$$

Fig. 7d shows permeability evolution from 300 to 340 K for three isobars. The permeability evolution follows the net aperture curves, with permeability enhancement following an inverted "U" shape due to permeability loss from thermal strain at higher temperatures. The isolated thermal permeability response in Fig. 7d is independent from pore

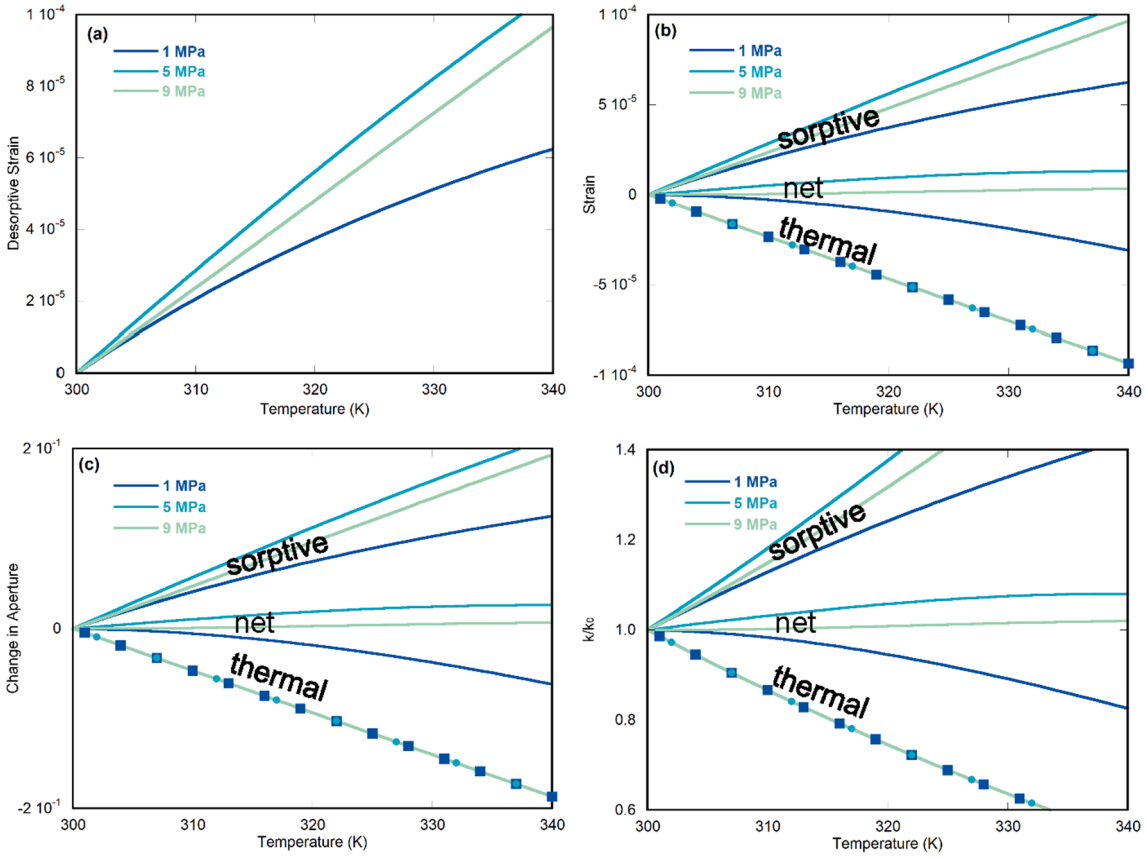

Fig. 7. The change in sorptive strain due to desorption from 300 K (a). The sorptive, thermal, and net strain (b). The sorptive, thermal, and net change in aperture (c). The sorptive, thermal, and net permeability evolution from 300 to 340 K.

pressure, suggesting that the permeability evolution will be positive or negative depending on the magnitude of the thermally induced desorption compared to the thermal strain.

Eq. (13) can be expanded using Eq. (5), Eq. (7) and Eq. (11) to explicitly cast isobars of permeability evolution in terms of changing temperatures:

$$\frac{k}{k_0} = (1 + A\frac{s}{b_0})\left(\varepsilon_L \frac{b_{\infty 0}\left(\frac{T}{T_0}\right)^{-\frac{1}{2}} \hat{A}\cdot e^{\frac{Q}{RT}}\hat{A}\cdot P}{1 + b_{\infty 0}\left(\frac{T}{T_0}\right)^{-\frac{1}{2}} \hat{A}\cdot e^{\frac{Q}{RT}}\hat{A}\cdot P} - \varepsilon_{s0} - \alpha_{th}\Delta T\right)^3 \quad (14)$$

where $\Delta\varepsilon_s$ has been separated into the sorptive strain at a given P,T and the initial sorptive strain ε_{s0}. As b_∞ varies with $T^{-1/2}$ for a given gas and solid, it is sufficient to measure or estimate the initial value $b_{\infty 0}$ and vary it accordingly.

3.3. Thermal-sorptive permeability model validation

We apply Eq. (14) to laboratory observations of permeability evolution in shales with varying temperature. There are several constants in Eq. (14) that should be measured in the laboratory or estimated from reported magnitudes. We estimate the heat of adsorption Q to be 17 kJ/mol, the Langmuir strain ε_L to be $5{\cdot}10^{-4}$, the coefficient of thermal expansion α_{th} to be $2{\cdot}10^{-5}$, and the Langmuir pressure P_L to be 6 MPa at 300 K [7,30,56,43]. With these values, we are able to isolate $b_{\infty 0}$ to be $1.83{\cdot}10^{-4}$ MPa^{-1} using Eq. (3) as:

$$P_L = \frac{1}{b} \rightarrow b_{\infty 0} = \left(\frac{1}{P_L}\right)\left(\frac{1}{e^{Q/RT}}\right) \quad (15)$$

We apply Eq. (14) to our experiments on the intact sample of Marcellus shale (MS1) and on the sample of Marcellus shale with a fracture of known dimensions (MS2). Fig. 8 shows all measurements that are conducted at a constant pore pressure of 6 MPa. Because data for MS1 is gathered at 6 MPa pore pressure, we include the four permeability measurements for MS2 that are also at 6 MPa pore pressure for comparison. For MS1, Eq. (14) fits the data when $A = 0.10$ and $s/b = 1{,}600$. For MS2, s/b was measured to be 16,500. Eq. (14) fits the data when $A = 0.06$. Fig. 8 shows the curves from Eq. (14) fit to both datasets. In both cases, permeability increases with increased thermally induced desorption. The fit data for MS1 show a rebound towards permeability

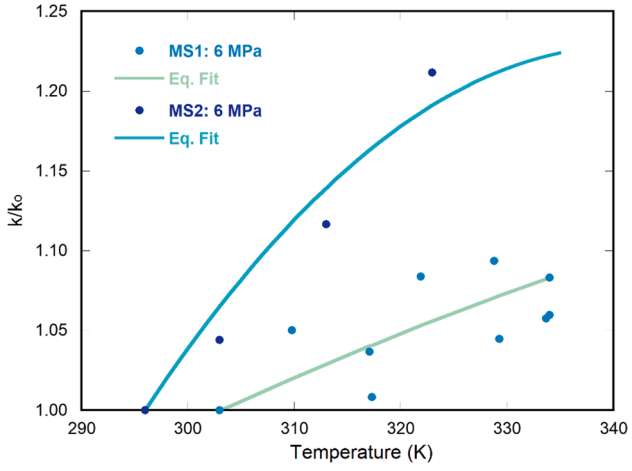

Fig. 8. Curve fits for Eq. (14) for a sample of intact Marcellus shale (MS1) and a sample of Marcellus shale with a fracture of known dimensions (MS2).

loss at ~ 335 K as thermal strain begins to outpace incremental desorption.

4. Discussion

We discuss the role of boundary conditions in determining the impact of the thermal strain and the role of mineral distribution in determining the difference between local and global strain. The role of fracture density is explored. The competition between sorptive and thermal strain is largest within the range of temperatures that typically exist within reservoirs. We explore the relationship between these strains and their impact on permeability evolution.

4.1. Boundary expansion

Eq. (14) accounts for the complete range of boundary conditions through application of the variable *A*. When *A* is equal to 1, the boundary is fixed such that any increase in grain volume decreases pore volume by the same amount. The Carman-Kozeny equation relates changes in permeability to changes in pore volume [3]. When porosity is low, the Carman-Kozeny equation is approximated as:

$$\frac{k}{k_0} \sim \left(\frac{\varphi}{\varphi_0}\right)^3. \tag{16}$$

Eq. (16) suggests that permeability decreases with grain volume expansion at constant bulk volume due to decreased pore volume.

At the opposite extreme of the spectrum, an unrestrained boundary that allows for free bulk volume expansion should result in a negligible impact on fracture aperture. In this case, thermal expansion of minerals results in an increased bulk volume instead of a decreased pore volume. When *A* is between 0 and 1, the thermal expansion partially expands the bulk volume and partially reduces the pore volume. Fig. 9 shows the impact of boundary expansion when varying *A* between 0 (free-expansion) and 1 (fully-constrained) at constant pore pressures of 1 MPa (Fig. 9a), 5 MPa (Fig. 9b), and 9 MPa (Fig. 9c).

While Eq. (9) and Eq. (10) assume that the volume expansion is determined by the boundary—by having the same *A* in both equations—it may not be reflective of how sorptive strain is distributed. Sorptive swelling in shales is not uniform within the matrix, which can cause a localized permeability response [61]. The %TOC in coals is generally between 50 and 80%, and the sorptive strain in coals is 10^{-2}. Shales typically have a lower %TOC—on the order of 1%-10%. However, for pore spaces concentrated near organic matter, the change in aperture caused by local swelling may be better modeled with a sorptive strain of 10^{-2}. In addition, shales are typically of lower fracture porosity and initial permeability, thus a relatively smaller change in strain can result in a relatively larger change in permeability [26]. Also, while clays are only slightly sorptive compared to organic matter, they also make up a larger volume percent of the shale. Flow paths have been shown to be concentrated in clays and organic matter in shales [52], which suggests that the local effect of desorption should be further studied.

4.2. Fracture density

Fractures that are spaced far apart have to accommodate more of the strain than when fractures are spaced close together [49]. In Eq. (12), the thermal strain and sorptive strain both change fracture aperture proportional to fracture spacing *s*. The pore deformation caused by either strain will be proportional to $s{\cdot}\varepsilon$ and in the case that $A = 1$, $\Delta b = s{\cdot}\varepsilon$ [2]. In Eq. (14), the change in aperture is proportional to s/b. The reciprocal of s/b is b/s, indicating the innate control of the proportionality of aperture to fracture density. For a given strain, a shale with a high fracture density will experience less change in permeability than a shale with low fracture density. Fig. 10 shows that fracture spacing influences permeability evolution in the same way that boundary expansion does. The main difference is that *A* ranges from 0 to 1, whereas s/b can be large. In MS2, s/b was 16,500. In MS1, s/b was approximately 1,600. This is consistent with other measurements for s/b in intact samples of Marcellus shale [49,50].

Eq. (14) is developed in such a way that A and s/b are both prefactors that act on the strain terms in the same way. While A and s/b are different physical characteristics of the system, they have the same scaling effect on permeability evolution. We note that both should be further constrained based on the needs of a particular project. In our case, we were able to measure s/b directly for MS1, reducing the uncertainty of our selection of A. We note that the A value for MS2 was similar to the A value for MS1, suggesting that A may be approximately 0.10 +/- 0.05 for shale systems described in this work. Similar methods can be used to minimize the uncertainty surrounding s/b. We note that s/b will vary spatially within a reservoir, and will vary based on the bedding direction that permeability is being measured in.

While fracture density can be simplified using b/s for our model input, we note that the development of porosity—especially in organic matter—is a complex process governed by pores on multiple scales. Organic pores in shale typically cannot be observed using SEM because they are smaller than 2 nm. However, macropores and microfissures found throughout clay material in shales are readily imaged using SEM. This interplay between a highly dense network of organic pores feeding into a sparse network of microfissures during transport is an area of ongoing research. We recommend that any practitioner needing to account for the impacts of nanoscale storage in organic matter include a separate fracture density term for this set of flow paths, use a field equation coupling Fickian and Darcian flow, and separating the model into directional flow and bedding-dependent permeability as appropriate to the specific case.

4.3. Sorptive and thermal strain

The competition between the sorptive and thermal strain creates a net change in permeability with an *inverted* "U" signature. Importantly,

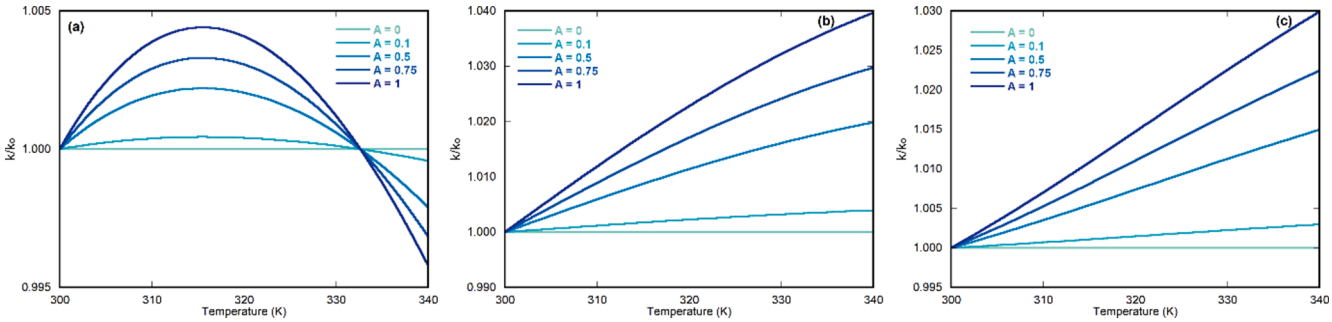

Fig. 9. The role of bulk volume expansion in determining permeability evolution due to thermal and sorptive strains. For free expansion (A = 0), permeability evolution is negligible. For fixed bulk volume (A = 1), permeability evolution is a function of competing thermal and sorptive strains.

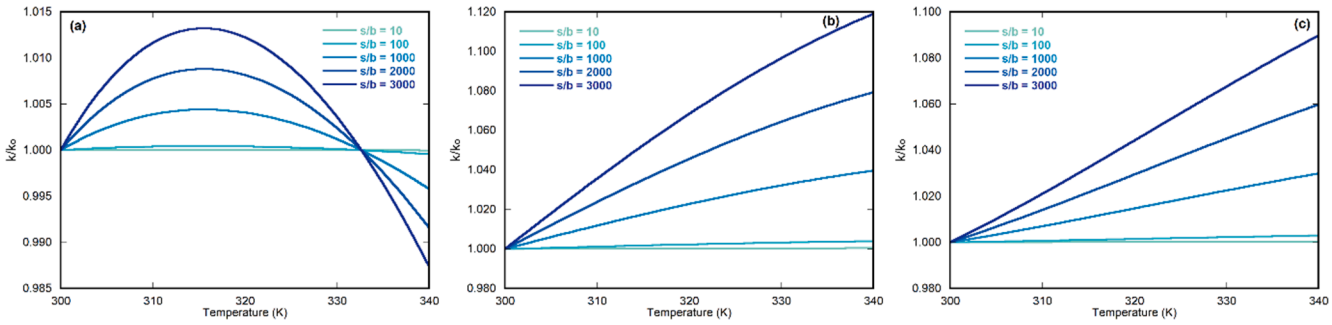

Fig. 10. The role of fracture spacing in determining permeability evolution at constant pore pressure for 1 MPa (a), 5 MPa (b), and 9 MPa (c).

the strains in Eq. (14) represent changes in strain from a reference temperature—in this case 300 K. While thermal strain is linear with ΔT in the 300–400 K range, the sorptive strain must be further constrained by the reference temperature. We do this by tracking $\Delta\varepsilon_s$ with ΔT and T_0. Thermal expansion in shales becomes nonlinear as temperature approaches 500 K. However, for small excursions in temperature and at temperatures typical of reservoirs, the thermal strain is linear. Fig. 11 shows changes in permeability evolution resulting from changing the coefficient of thermal expansion. For lower values of α_{th}, permeability experiences a larger enhancement.

Sorptive strains in shale are typically on the order of 10^{-4}. Maximum sorptive capacity has been shown to decrease with temperature [60], suggesting that the maximum sorptive strain ε_L could also change. Fig. 12 shows how sorptive capacity of a shale influences its permeability evolution relative to the thermal strain. For the 1 MPa isobar, the 10^{-4} Langmuir strain is insufficient to overcome the permeability loss due to mineral expansion. Referring to Fig. 6c, this is due to the majority of the thermally-induced desorption occurring at temperatures lower than 300 K at a pore pressure of 1 MPa. Fig. 12(b-c) show that the permeability enhancement for the 5 MPa and 9 MPa isobars can be substantial. The largest Langmuir strain considered in Fig. 12 is 10^{-3}, which is an order of magnitude larger than bulk sorptive strains typically measured in shales. However, it may be that a sorptive strain of 10^{-3} is too small to model fracture expansion caused by shrinkage of clays and organic matter immediately surrounding fractures and micro-fissures. In such a case, the local effect of fracture expansion due to reduced swelling may be better modeled with a sorptive strain of 10^{-2}. Compared to the coefficient of thermal expansion for organic matter of 10^{-5}, the local effect of a 10^{-2} relaxation of the sorptive strain could lead to substantial permeability enhancement. This observation is consistent with the notion of an internal strain that impacts pore dilation and is proportional to the volumetric swelling strain in shales [40].

Fig. 13 shows three regions on a normalized permeability vs. temperature plot that compares thermal to sorptive strains. In general, the change in sorptive strain is larger than thermal strain at lower temperatures but smaller at higher temperatures. Fig. 6 and Fig. 7a show that desorption at higher temperature flattens out much like Langmuir isotherms do at higher pressure. For a standard isobar generated by Eq. (14), normalized permeability would begin in the top region of Fig. 13 where desorption outpaces thermal expansion. Once the two strains approach similar values, the permeability curve would rebound. As linear thermal expansion begins to outpace incremental desorption with increased temperature, permeability will decrease.

The net permeability response depends on which strain is larger: thermal or sorptive. Therefore, a ratio of changing sorptive strain to changing thermal strain can be developed:

$$R = \frac{\Delta\varepsilon_s}{\Delta\varepsilon_{th}} \tag{17}$$

When R is greater than 1, permeability increases and when R is less than 1, permeability decreases. Normalized permeability is plotted against temperature for various isobars in Fig. 14a. For pore pressures less than 1 MPa, permeability monotonically decreases as there is insufficient incremental desorption to overcome permeability loss from mineral expansion. Pore pressures between 1 and 2 MPa return an inverted "U" shaped permeability evolution indicative of early permeability enhancement from desorption being finally outpaced by permeability loss from mineral expansion at higher temperatures. Pore pressures greater than 2 MPa show monotonically increasing permeability as the fractional coverage of sorption sites changes by a substantial margin within the temperature range of the plot. At higher temperatures, however, permeability will begin to decrease as there is no meaningful change in incremental sorptive strain to overcome permeability loss from continued linear expansion of the mineral matter.

Fig. 14b shows the same permeability isobars plotted vs. the R values from Eq. (17) for each data point. When R is less than 1, permeability decreases. When R equals 1, permeability does not change. When R is greater than 1, permeability in enhanced. As R becomes much smaller or much greater than 1, the magnitude of permeability fluctuation becomes large. Eq. (17) can be expanded to highlight that for a given gas and solid, R changes due to changing temperature and changing fractional coverage:

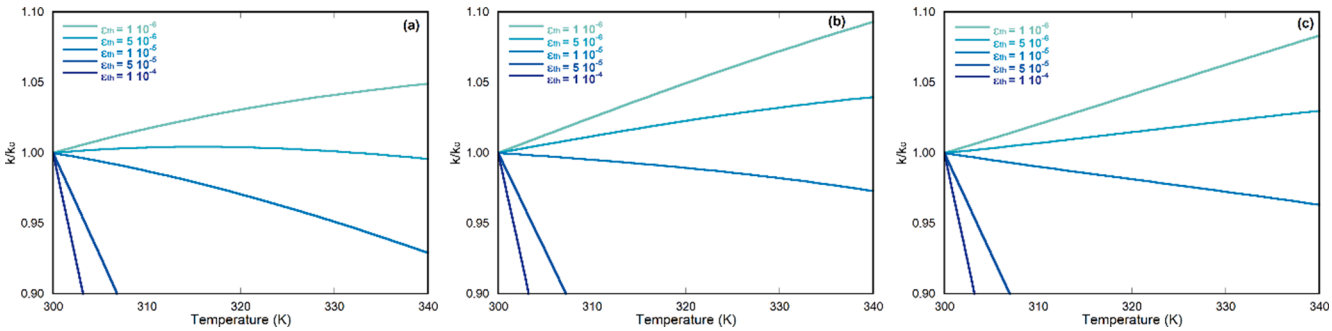

Fig. 11. The role of the coefficient of thermal expansion on permeability evolution at constant pore pressure isobars of 1 MPa (a), 5 MPa (b), and 9 MPa (c). As α_{th} becomes smaller, the permeability enhancement due to desorption becomes the dominant strain.

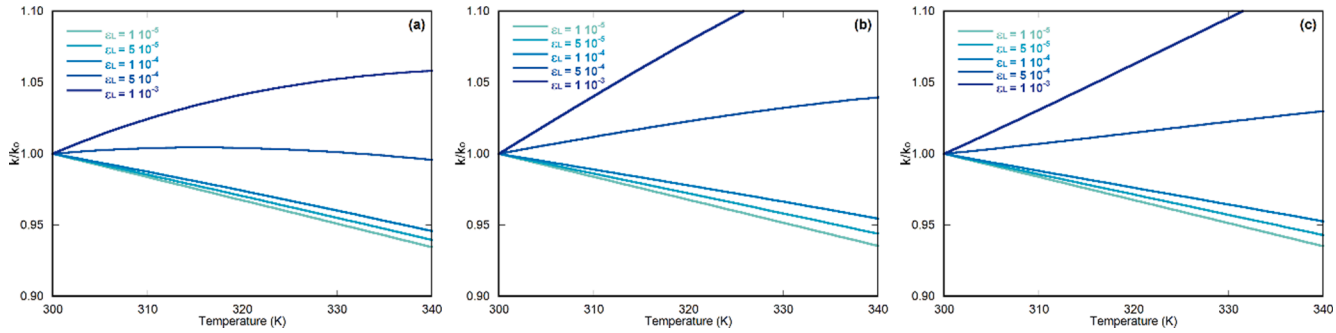

Fig. 12. The role of maximum sorptive strain on permeability evolution at constant pore pressure isobars of 1 MPa (a), 5 MPa (b), and 9 MPa (c).

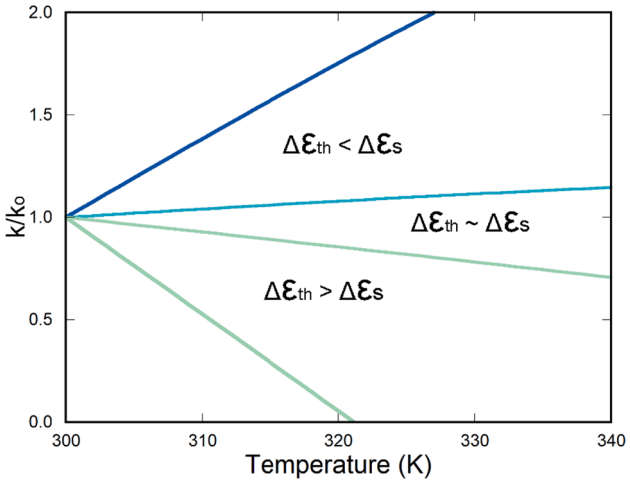

Fig. 13. Regions of permeability evolution based on the competition between evolving sorptive and thermal strains. At temperatures close to T_0 permeability increases due to the dominance of desorption. Sorptive strain becomes nonlinear at higher temperatures (relative to T_0) resulting in permeability loss as the impact of linear thermal expansion reduces pore volume.

$$R = \frac{\varepsilon_L}{\frac{1}{3}\alpha_{th}} \frac{\Delta\theta}{\Delta T} \tag{18}$$

where ε_L and α_{th} are constants that condition the magnitude of R but do not cause R to change.

5. Conclusions

Permeability evolution at constant pore pressure and varying temperature can be represented then modeled as the net response to two competing strains. Sorptive strain is competitive with thermal strain, where desorption causes permeability enhancement and thermal expansion of the mineral aggregate causes permeability loss. Both strains are distributed between boundary expansion of the bulk volume and reduction of pore volume and conditioned by the associated conditions of boundary constraint. The change in fracture aperture is directly impacted by fracture density.

Both thermal and sorptive strains are modulated by the mineral distribution within the shale. These minerals have different coefficients of thermal expansion and different sorptive capacities. Whereas clays are only slightly sorptive compared to the organic matter, clays also make up a much larger volume percent of the shale and thus are important in their contribution to overall strain. Silicates and carbonates are nonsorptive. Organic matter and clays also have higher coefficients of thermal expansion compared to silicates and carbonates. This may indicate a partitioned, localized permeability response within clays and organic matter experiencing thermal and sorptive strains.

Thermally induced desorption at constant pore pressure can be modeled using the Langmuir adsorption model. Compared to the "U" shape of permeability curves for sorptive rocks with increasing pore pressure, our model for permeability evolution has an inverted "U" shape with increasing temperature. Permeability enhancement at

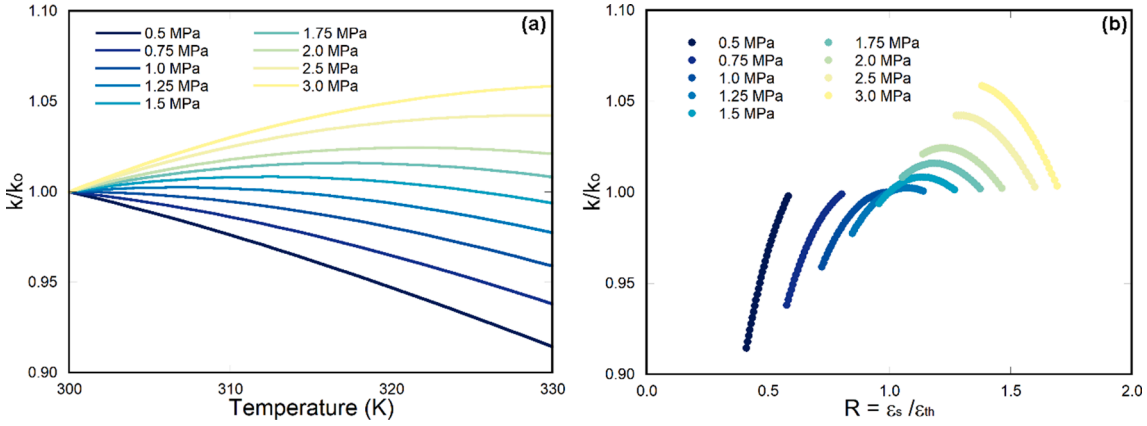

Fig. 14. Permeability evolution for various isobars. (a) shows the transition from increasing permeability to decreasing permeability as isobars of pore pressure change. (b) shows the impact of R on the magnitude of permeability evolution.

temperatures close to the initial reservoir temperature are eventually outpaced by permeability loss at higher temperatures. This is due to thermal strain being linear from 300 to 400 K whereas the increment of sorptive strain diminishes as temperature continues to increase. When the sorptive strain is much larger than the thermal strain, as captured by the ratio between them being much greater than one ($R \gg 1$), the permeability of the shale will increase significantly. In addition, the ratio between the sorptive strain and the thermal strain can be used to predict the magnitude and sign of permeability evolution. As either the thermal strain or sorptive strain becomes much larger than the other, permeability fluctuation becomes large.

There may be local desorption which has a larger impact than the bulk sorptive strain suggests. Quantifying the net system response of adsorption on different minerals can be estimated using bulk measurements as we do here. To quantify the local influence of mineral distribution on the sorptive strain would require micromechanical modeling, which we suggest as a future study to build from this work. We also recommend further study into the distribution of the sorptive strain and its impact on nearby flow channels.

CRediT authorship contribution statement

Brandon Schwartz: Conceptualization, Data curation, Formal analysis, Investigation, Methodology, Software, Validation, Writing - original draft. **Derek Elsworth:** Conceptualization, Formal analysis, Funding acquisition, Investigation, Methodology, Project administration, Resources, Supervision.

Declaration of Competing Interest

The authors declare that they have no known competing financial interests or personal relationships that could have appeared to influence the work reported in this paper.

Acknowledgements

This work is a partial result of support from Chevron Energy Technology Company, and their support is gratefully acknowledged.

References

[1] Bai M, Elsworth D, Roegiers J-C. Multiporosity/multipermeability approach to the simulation of naturally fractured reservoirs. Water Resour Res 1993;29(6):1621–33.
[2] Bai M, Elsworth D. Coupled processes in subsurface deformation, flow, and transport. American Society of Civil Engineers; 2000. p. 107.
[3] Bear J. Dynamics of fluids in porous media. Courier Corporation. 2013.
[4] Bolton AJ, Maltman AJ, Fisher Q. Anisotropic permeability and bimodal pore-size distributions of fine-grained marine sediments. Marine Petroleum Geology 2000;17(6):657–72.
[5] Cao P, Liu J, Leong Y-K. A multiscale-multiphase simulation model for the evaluation of shale gas recovery coupled the effect of water flowback. Fuel 2017;199:191–205.
[6] Chen L, Zhang L, Kang Q, Viswanathan HS, Yao J, Tao W. Nanoscale simulation of shale transport properties using the lattice Boltzmann method: permeability and diffusivity. Nature Scientific Reports 2015;5(1):1–8.
[7] Chen L, Zuo L, Jiang Z, Jiang S, Liu K, Tan J, et al. Mechanisms of shale gas adsorption: Evidence from thermodynamics and kinetics study of methane adsorption on shale. Chem Eng J 2019;361:559–70.
[8] Civan F, Rai CS, Sondergeld CH. (2012) Determining shale permeability to gas by simultaneous analysis of various pressure tests. SPE Journal,17(03):717–26.
[9] Closmann PJ, Bradley WB. The effect of temperature on tensile and compressive strengths and Young's modulus of oil shale. Soc Petrol Eng J 1979;19(05):301–12.
[10] Cooper HW, Simmons G. The effect of cracks on the thermal expansion of rocks. Earth Planet Sci Lett 1977;36(3):404–12.
[11] Curtis, M. E., Sondergeld, C. H., and Rai, C. S. (2019, October). Visualization of Pore Connectivity Using Mercury Injection Capillary Pressure Measurements, Micro X-ray Computed Tomography, and Cryo Scanning Electron Microscopy. In URTeC, Denver, Colorado, 22-24 July 2019 (pp. 3143-3154). (URTeC); Society of Exploration Geophysicists.
[12] Curtis ME, Sondergeld CH, Ambrose RJ, Rai CS. (2012) Microstructural investigation of gas shales in two and three dimensions using nanometer-scale resolution imaging Microstructure of Gas Shales. AAPG Bulletin 2012;96(4):665–77.
[13] Daigle H, Hayman NW, Kelly ED, Milliken KL, Jiang H. Fracture capture of organic pores in shales. Geophys Res Lett 2017;44(5):2167–76.
[14] Do DD. Adsorption Analysis: Equilibria and Kinetics, Vol. 2. World Scientific; 1998.
[15] Fan D, Ettehadtavakkol A. Analytical model of gas transport in heterogeneous hydraulically-fractured organic-rich shale media. Fuel 2017;207:625–40.
[16] Gilliam, T. M., and Morgan, I. L. (1987). Shale: Measurement of thermal properties (No. ORNL/TM-10499). Oak Ridge National Lab., TN (USA).
[17] Goral J, Walton I, Andrew M, Deo M. Pore system characterization of organic-rich shales using nanoscale-resolution 3D imaging. Fuel 2019;258:116049. https://doi.org/10.1016/j.fuel.2019.116049.
[18] Gu X, Mildner DFR. Ultra-small-angle neutron scattering with azimuthal asymmetry. J Appl Crystallogr 2016;49(3):934–43.
[19] Horne SA. A statistical review of mudrock elastic anisotropy. Geophys Prospect 2013;61(4):817–26.
[20] Izadi G, Wang S, Elsworth D, Liu J, Wu Yu, Pone D. Permeability evolution of fluid-infiltrated coal containing discrete fractures. Int J Coal Geol 2011;85(2):202–11.
[21] Javadpour F, Fisher D, Unsworth M. Nanoscale gas flow in shale gas sediments. J Can Pet Technol 2007;46(10).
[22] Javadpour F. Nanopores and apparent permeability of gas flow in mudrocks (shales and siltstone). J Can Pet Technol 2009;48(08):16–21.
[23] Kang SM, Fathi E, Ambrose RJ, Akkutlu IY, Sigal RF. Carbon dioxide storage capacity of organic-rich shales. SPE J 2011;16(4):842–55.
[24] Keller LM, Holzer L, Wepf R, Gasser P. 3D geometry and topology of pore pathways in Opalinus clay: Implications for mass transport. Appl Clay Sci 2011;52(1-2):85–95.
[25] Khan MR, Jenkins RG. Thermoplastic properties of coal at elevated pressures: 1. Evaluation of a high-pressure microdilatometer. Fuel 1984;63(1):109–15.
[26] Kumar H, Elsworth D, Mathews JP, Marone C. Permeability evolution in sorbing media: analogies between organic-rich shale and coal. Geofluids 2016;16(1):43–55.
[27] Kwon O, Kronenberg AK, Gangi AF, Johnson B, Herbert BE. Permeability of illite-bearing shale: 1. Anisotropy and effects of clay content and loading. Journal of Geophysical Research: Solid. Earth 2004;109(B10).
[28] Levine JR. Model study of the influence of matrix shrinkage on absolute permeability of coal bed reservoirs. Geological Society, London, Special Publications 1996;109(1):197–212.
[29] Li J, Chen Z, Wu K, Wang K, Luo J, Feng D, et al. A multi-site model to determine supercritical methane adsorption in energetically heterogeneous shales. Chem Eng J 2018;349:438–55.
[30] Li X, Elsworth D. Geomechanics of CO2 enhanced shale gas recovery. J Nat Gas Sci Eng 2015;26:1607–19.
[31] Li, Z. Q., Xian, X. F., and Long, Q. M. (2009). Experiment Study of Coal Permeability Under Different Temperature and Stress. Journal of China University of Mining and Technology, 04.
[32] Li Z, Elsworth D. Controls of CO2–N2 gas flood ratios on enhanced shale gas recovery and ultimate CO2 sequestration. J Petrol Sci Eng 2019;179:1037–45.
[33] Liu H-H, Rutqvist J. A new coal-permeability model: internal swelling stress and fracture–matrix interaction. Transp Porous Media 2010;82(1):157–71.
[34] Liu J, Chen Z, Elsworth D, Qu H, Chen D. Interactions of multiple processes during CBM extraction: a critical review. Int J Coal Geol 2011;87(3-4):175–89.
[35] Liu, Q., Cheng, Y., Dong, J., Liu, Z., Zhang, K., and Wang, L. (2018). Non-Darcy Flow in Hydraulic Flushing Hole Enlargement-Enhanced Gas Drainage: Does It Really Matter?. Geofluids, 2018.
[36] Liu S, Harpalani S. A new theoretical approach to model sorption-induced coal shrinkage or swelling. AAPG Bull 2013;97(7):1033–49.
[37] Lu XC, Li FC, Watson AT. Adsorption measurements in Devonian shales. Fuel 1995;74(4):599–603.
[38] Marschall P, Horseman S, Gimmi T. Characterisation of gas transport properties of the Opalinus Clay, a potential host rock formation for radioactive waste disposal. Oil and Gas Science and Technology 2005;60(1):121–39.
[39] Pan Z, Ma Y, Connell LD, Down DI, Camilleri M. Measuring anisotropic permeability using a cubic shale sample in a triaxial cell. J Nat Gas Sci Eng 2015;26:336–44.
[40] Peng Y, Liu J, Pan Z, Qu H, Connell L. Evolution of shale apparent permeability under variable boundary conditions. Fuel 2018;215:46–56.
[41] Qu, H. Y., Liu, J. S., Pan, Z. J., and Connell, L. (2010, June). Impact of thermal processes on CO2 injectivity into a coal seam. In IOP Conference Series: Materials Science and Engineering (Vol. 10, No. 1, p. 012090). IOP Publishing.
[42] Qu H, Liu J, Chen Z, Wang J, Pan Z, Connell L, et al. Complex evolution of coal permeability during CO2 injection under variable temperatures. Int J Greenhouse Gas Control 2012;9:281–93.
[43] Robertson, E. C. (1988) Thermal properties of rocks. United States Department of the Interior Geological Survey.
[44] Robertson, E. P. (2005). Measurement and modeling of sorption-induced strain and permeability changes in coal (No. INL/EXT-06-11832). Idaho National Laboratory (INL).
[45] Rybacki E, Meier T, Dresen G. What controls the mechanical properties of shale rocks?–Part II: Brittleness. J Petrol Sci Eng 2016;144:39–58.
[46] Sakurovs R, Day S, Weir S, Duffy G. Temperature dependence of sorption of gases by coals and charcoals. Int J Coal Geol 2008;73(3-4):250–8.
[47] Schwartz B, Huffman K, Thornton D, Elsworth D. A strain based approach to calculate disparities in pore structure between shale basins during permeability evolution. J Nat Gas Sci Eng 2019;68:102893. https://doi.org/10.1016/j.jngse.2019.05.006.

[48] Schwartz B, Elsworth D, Marone C. Relationships between mechanical and transport properties in Marcellus shale. Int J Rock Mech Min Sci 2019;119:205–10.
[49] Schwartz B, Huffman K, Thornton D, Elsworth D. The effects of mineral distribution, pore geometry, and pore density on permeability evolution in gas shales. Fuel 2019;257:116005. https://doi.org/10.1016/j.fuel.2019.116005.
[50] Schwartz B, Elsworth D. A strain-based model for recovering sorptive permeability loss observed in laboratory experiments of shale. Journal of Petroleum Science and Engineering. In review. 2021.
[51] Sinha S, Braun EM, Determan MD, Passey QR, Leonardi SA, Boros JA, et al. March). Steady-state permeability measurements on intact shale samples at reservoir conditions-effect of stress, temperature, pressure, and type of gas. Society of Petroleum Engineers; 2013.
[52] Slatt RM, O'Brien NR. Pore types in the Barnett and Woodford gas shales: Contribution to understanding gas storage and migration pathways in fine-grained rocks. AAPG Bull 2011;95(12):2017–30.
[53] Sondergeld, C. H., Newsham, K. E., Comisky, J. T., Rice, M. C., and Rai, C. S. (2010, January). Petrophysical considerations in evaluating and producing shale gas resources. In SPE Unconventional Gas Conference. Society of Petroleum Engineers.
[54] Sone H, Zoback MD. Mechanical properties of shale-gas reservoir rocks—Part 1: Static and dynamic elastic properties and anisotropy. Geophysics 2013;78(5): D381–92.
[55] Ulm F-J, Abousleiman Y. The nanogranular nature of shale. Acta Geotech 2006;1 (2):77–88.
[56] Vermylen JP. Geomechanical studies of the Barnett shale, Texas. USA: Stanford University; 2011.
[57] Wang S, Elsworth D, Liu J. A mechanistic model for permeability evolution in fractured sorbing media. J Geophys Res Solid Earth 2012;117(B6).
[58] Witherspoon PA, Wang JSY, Iwai K, Gale JE. Validity of cubic law for fluid flow in a deformable rock fracture. Water Resour Res 1980;16(6):1016–24.
[59] Wu K, Chen Z, Li X, Guo C, Wei M. A model for multiple transport mechanisms through nanopores of shale gas reservoirs with real gas effect–adsorption-mechanic coupling. Int J Heat Mass Transf 2016;93:408–26.
[60] Ye Z, Chen D, Pan Z, Zhang G, Xia Y, Ding X. An improved Langmuir model for evaluating methane adsorption capacity in shale under various pressures and temperatures. J Nat Gas Sci Eng 2016;31:658–80.
[61] Zeng J, Liu J, Li W, Leong Y-K, Elsworth D, Guo J. Evolution of shale permeability under the influence of gas diffusion from the fracture wall into the matrix. Energy Fuels 2020;34(4):4393–406.
[62] Zhou S, Wang H, Zhang P, Guo W. Investigation of the isosteric heat of adsorption for supercritical methane on shale under high pressure. Adsorpt Sci Technol 2019; 37(7-8):590–606.
[63] Zhu C, Arson C. A thermo-mechanical damage model for rock stiffness during anisotropic crack opening and closure. Acta Geotech 2014;9(5):847–67.